H and Cl isotope characteristics of indigenous and late hydrothermal fluids on the differentiated asteroidal parent body of Grave Nunataks 06128

Journal Item

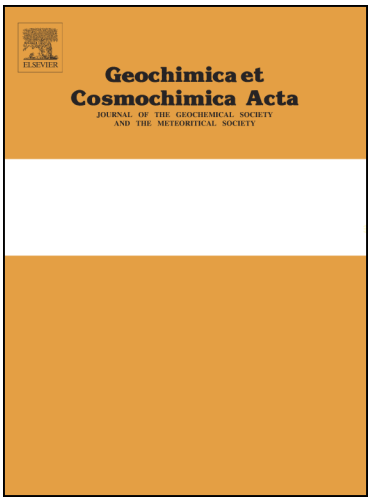

H and Cl isotope characteristics of indigenous and late hydrothermal fluids on the differentiated asteroidal parent body of Grave Nunataks 06128

Romain Tartèse, Mahesh Anand, Ian A. Franchi

PII: S0016-7037(19)30047-X
DOI: https://doi.org/10.1016/j.gca.2019.01.024
Reference: GCA 11097

To appear in: *Geochimica et Cosmochimica Acta*

Received Date: 10 May 2018
Revised Date: 4 November 2018
Accepted Date: 15 January 2019

Please cite this article as: Tartèse, R., Anand, M., Franchi, I.A., H and Cl isotope characteristics of indigenous and late hydrothermal fluids on the differentiated asteroidal parent body of Grave Nunataks 06128, *Geochimica et Cosmochimica Acta* (2019), doi: https://doi.org/10.1016/j.gca.2019.01.024

H and Cl isotope characteristics of indigenous and late hydrothermal fluids on the differentiated asteroidal parent body of Grave Nunataks 06128

Romain Tartèse[a*], Mahesh Anand[b,c], and Ian A. Franchi[b]

[a]School of Earth and Environmental Sciences, The University of Manchester, Manchester, M13 9PL, UK.

[b]School of Physical Sciences, The Open University, Milton Keynes MK7 6AA, UK.

[c]Department of Earth Sciences, The Natural History Museum, Cromwell Road, London, SW7 5BD, UK.

*Corresponding author: R. Tartèse (romain.tartese@manchester.ac.uk)

Abstract

The paired achondrites Graves Nunataks (GRA) 06128 and 06129 are samples of an asteroid that underwent partial melting within a few million years after the start of Solar System formation. In order to better constrain the origin and processing of volatiles in the early Solar System, we have investigated the abundance of H, F and Cl and the isotopic composition of H and Cl in phosphates in GRA 06128 using secondary ion mass spectrometry. Indigenous H in GRA 06128, as recorded in magmatic merrillite, is characterised by an average δD of *ca*. -152 ± 330‰, which is broadly similar to estimates of the H isotope composition of indigenous H in other differentiated asteroidal and planetary bodies such as Mars, the Moon and the angrite and eucrite meteorite parent bodies. The merrillite data thus suggest that early accretion of locally-derived volatiles was widespread for the bodies currently populating the asteroid belt. Apatite formed at the expense of merrillite around 100 million years after the differentiation of the GRA 06128/9 parent body, during hydrothermal alteration, which was probably triggered by an impact event. Apatite in GRA 06128 contains 5.4-5.7 wt.% Cl, 0.6-0.8 wt.% F, and ~20 to 60 ppm H_2O, which is similar to the H_2O abundance in merrillite from which apatite formed. The apatite δD values range between around +100‰ and +2000‰ and are inversely correlated with apatite H_2O contents. The Cl isotope composition of apatite appears to be homogeneous across various grains, with an average $\delta^{37}Cl$ value of 3.2 ± 0.7‰. A possible scenario to account for the apatite chemical and isotopic characteristics involves interaction of GRA 06128/9 with fumarole-like fluids derived from D- and HCl-rich ices delivered to the GRA 06128/9 parent-body by an ice-rich impactor.

Keywords

Apatite; Merrillite; Asteroids; H isotopes; Cl isotopes; Secondary Ion Mass Spectrometry

1. Introduction

Light volatile elements such as H, C, N and O compose most of the chemical species present in proto-planetary systems (e.g., Pontoppidan et al., 2014, and references therein). They are, therefore, key to understanding the processes involved in the formation and evolution of the earliest cometary and asteroidal bodies in solar systems. Larger rocky planetary bodies, such as the Earth, Venus or Mars, formed in warm inner regions of the Solar System and are thought to have largely accreted dry (e.g., Albarède, 2009) despite evidence for the presence of water (and other volatiles) in their interiors (e.g., Lécuyer et al., 1998; Hallis et al., 2012; Marty, 2012; McCubbin et al., 2012; Usui et al., 2012; Halliday, 2013). To better understand the origin and delivery timescales for volatiles in the inner Solar System objects, a more comprehensive inventory of their distribution and isotopic composition in cometary and asteroidal objects is needed. In addition, better understanding of the effects of ubiquitous processes, such as partial melting, impact processes, and hydrothermal alteration on the volatile inventory of asteroidal material is needed to disentangle primary and secondary signatures.

Because they are thought to be the most primitive objects in our Solar System, chondritic meteorites have been the focus of most sample studies on volatiles (see for example Alexander et al., 2012; Marty, 2012; Halliday, 2013; Scott and Krot, 2014). Our understanding of the volatile inventory and processing in the early Solar System is thus *de-facto* incomplete, as volatiles such as H, C and N in many achondritic early-formed rocky objects have not yet been investigated fully, except for samples from the Howardite-Eucrite-Diogenite (HED), angrite and ureillite parent bodies (e.g., Grady et al., 1985, 1997; Rai et al., 2003; Abernethy et al., 2013; Sarafian et al., 2014, 2017a, 2017b, 2017c; Downes et al., 2015; Barrett et al., 2016; Barrat et al., 2017). Differentiated achondrites are derived from

fully melted parent-bodies (e.g., Greenwood et al., 2005). Some of them, such as the HED meteorites, which likely originate from the asteroid 4-Vesta and Vesta-type smaller bodies (e.g., McCord et al., 1970), formed within ~10-20 million years (Ma) of Solar System formation (Misawa et al., 2005; Zhou et al., 2013) and are characterized by Earth-like H, C and N isotopic compositions (Miura and Sugiara, 1993; Grady et al., 1997; Grady and Wright, 2003; Sarafian et al., 2014; Barrett et al., 2016). Other early-formed achondrites are products and residues of low degrees of partial melting of chondritic precursors formed during the first few million years of Solar System history due to decay of short-lived radioisotopes such as ^{26}Al (e.g., Lee et al., 1976; LaTourette and Wasserburg, 1998; Weiss and Elkins-Tanton, 2013). They, therefore, constitute ideal targets to complement our biased knowledge regarding the origin and processing of volatiles in the early Solar System.

Graves Nunataks (GRA) 06128 and 06129 (referred as GRA 06128/9 in the following) are two paired achondrite meteorites recovered from Antarctica in 2006 (e.g., Day et al., 2009, 2012; Shearer et al., 2010). With a bulk andesitic composition, GRA 06128/9 is unique among the meteorite collection and has challenged the paradigm that all early asteroidal crusts were basaltic (Day et al., 2009; Shearer et al., 2010). GRA 06128/9 is characterised by > 70 modal % of sodic plagioclase, Fe-rich pyroxene (both high- and low-Ca) and olivine, sulfides, Fe-Ni-metal and the two phosphates merrillite and apatite (Fig. 1) (e.g., Day et al., 2009, 2012; Shearer et al., 2010, 2011; Zhou et al., 2018). Several geochemical characteristics, such as O and Fe isotope systematics (Day et al., 2012; Greenwood et al., 2012; Wang et al., 2014) and highly siderophile element (HSE) abundances (Day et al., 2012), suggest that GRA 06128/9 and the brachinite meteorites originated from the same asteroidal parent-body. An Al-Mg model age suggests that GRA 06128/9 formed ~4565 Ma ago (Shearer et al., 2010), within 2-3 million years of the formation of the Solar System.

After its formation, GRA 06128/9 has recorded a complex history of re-heating and subsolidus alteration that lasted for up to *ca*. 300 Ma (Day et al., 2009; Shearer et al., 2010, 2011; Lindsay et al., 2014; Claydon et al., 2015; Zhou et al., 2018), and which included (i) subsolidus re-equilibration of silicates, oxides, and sulfides, (ii) impact-triggered development of granoblastic textures, and (iii) alteration and transformation of merrillite (± pyroxene) into chlorapatite by Cl-rich fluids.

The recent U-Pb chronological data obtained by Zhou et al. (2018) yielded an apatite $^{207}Pb/^{206}Pb$ weighted average date of 4460 ± 30 Ma (2σ), which is significantly younger than the Al-Mg model age for crystallisation of GRA 06128/9. This apatite Pb/Pb date is also significantly younger than the $^{207}Pb/^{206}Pb$ weighted average date of 4578 ± 48 Ma (2σ) that can be calculated using only the five merrillite analyses given in Day et al. (2009). This merrillite Pb/Pb date is identical within errors to the Al-Mg formation age of ~4565 Ma for GRA 06128/9, while the apatite Pb/Pb date is consistent with an Ar/Ar date interpreted as a resetting age (Shearer et al., 2010; Claydon et al., 2015). Pb/Pb dating studies thus confirm the initial suggestion of Shearer et al. (2011) that merrillite is the primary magmatic phosphate in GRA 06128/9 and that Cl-rich apatite formed later in response to the interaction between merrillite and Cl-rich fluids. The volatile inventory of merrillite should thus provide constraints on that of the partial melts from which GRA 06128/9 crystallized within 2-3 million years after the start of Solar System formation, while the apatite volatile inventory should yield valuable information on the metasomatic fluids that circulated on the GRA 06128/9 parent-body ~100 million years after its formation.

2. Material and methods

2.1. Scanning electron microscopy

The studied polished section of GRA 06128 (Fig. 1) was prepared at NASA Johnson Space Center in a water-free medium and mounted onto a glass plate using araldite epoxy. It was carbon coated and examined using a Quanta 3D Focused Ion Beam Scanning Electron Microscope (FIB-SEM) at the Open University, fitted with an Oxford Instruments INCA energy dispersive X-ray detector, and using an electron beam with an acceleration voltage of 20 kV. To locate phosphate grains in the polished section, back-scatter electron (BSE) images and X-ray maps of the whole section were obtained by energy dispersive spectroscopy (EDS). Phosphates were located using P X-ray maps of the section. High magnification BSE imaging and quick acquisition of X-ray spectra for ~15 s permitted distinction between apatite and merrillite without generating electron beam-induced volatile mobility in apatite (e.g., Barnes et al., 2013). Isopropanol was subsequently used for removing carbon coating from the samples in preparation for ion probe work.

Location of Figure 1

2.2. Secondary ion mass spectrometry (SIMS)

2.2.1. H_2O abundance and H isotope analysis

The H_2O abundance and H isotope composition of phosphates were measured using the CAMECA NanoSIMS 50L at the Open University, following a well-established protocol described in detail in Barnes et al. (2013, 2014) and Tartèse et al. (2013). In brief, analyses were carried out using a large Cs^+ primary beam of ~ 280 pA current, with an accelerating voltage of 16 kV, after a 3 minutes pre-sputter during which the beam was rastered on the sample surface over 12 µm × 12 µm areas to eliminate any surface contamination. Secondary ions of ^1H, ^2H, ^{12}C and ^{18}O were collected simultaneously on electron multipliers for 2000 cycles (~20 min) from the inner 25 % area of 10 µm × 10 µm rasters using electronic gating.

An electron gun was used for charge compensation and tuned to minimise its contribution to the H background. The mass resolving power was set to ~4000 (CAMECA definition) to resolve D^+ from the interfering H_2^+ species. Secondary ion images of ^1H and ^{12}C were monitored in real time during pre-sputtering to ensure that the analysed areas were free of any surficial contamination, cracks or hotspots. The vacuum in the analysis chamber was ~3-5 × 10^{-10} torr.

Apatite and merrillite H_2O contents were calibrated using the measured $^1H/^{18}O$ ratio and the calibrations derived using terrestrial apatite standards (Atlas Mountain apatite Ap004, Crystal Lode Pegmatite Mine apatite Ap005, Lake Baikal apatite Ap018 and Indian pegmatite apatite Ap020, all described in McCubbin et al., 2012) pressed in indium along with a San Carlos olivine crystal. The reported uncertainties on H_2O contents combine the 2σ uncertainty associated with the calibration line and the analytical uncertainties associated with each individual measurement. A chip of nominally anhydrous San Carlos olivine (H_2O ~ 0.0001 wt.%; Aubaud et al., 2007) was used to calculate an instrumental H_2O background of 16 ± 11 ppm H_2O (2SD, n = 16). To ensure that this measure was adequate for epoxy-mounted samples such as GRA 06128, analyses were also carried out under our routine analytical conditions in silica in a eucrite thin section analysed during the same analytical session. These analyses yielded ~20 ± 8 ppm H_2O (2SD, n = 2), which is comparable to the background H_2O determined on the indium-mounted San Carlos olivine. This is also consistent with H_2O contents of ~10 ppm measured in olivine and plagioclase, in lunar troctolite 76535 by Barnes et al. (2014) using the same instrument and analytical protocol, which these authors interpreted as instrumental background H_2O. This background H_2O content was subtracted from the H_2O contents measured in GRA 06128 phosphates. Instrumental background H_2O contributed to the measured D/H ratios, since background H_2O

represents 23 to 46% of the total H measured for all GRA 06128 phosphate analyses (Table 1). The raw D/H ratios measured on GRA 06128 phosphates were, therefore, corrected for instrumental background contribution, which we calculated to be $3.96\times10^{-4} \pm 0.85\times10^{-4}$ (95% confidence level, MSWD = 2.2) based on nine analyses of San Carlos olivine carried out just before, during, and just after the GRA 06128 phosphate analyses, following the relationship:

$$D/H_{measured} = f \times D/H_{phosphate} + (1 - f) \times D/H_{background},$$

where f is the proportion of H emitted from the phosphates. The raw D/H ratios along with the background corrected D/H ratios are listed in Table 1.

A reference apatite, Ap004 (δD = -45 ± 5‰, McCubbin et al., 2012), was used to correct the background corrected D/H ratios from instrumental mass fractionation (IMF; 395 ± 21‰ during the analytical session). The accuracy of our D/H measurements was checked and validated by repeated measurements on additional reference apatite samples treated as unknowns. Apatite samples Ap005 (0.37 wt.% H_2O & δD = -73 ± 4‰, McCubbin et al., 2012) and Ap018 (0.20 wt.% H_2O & δD = -90 ± 14‰, McCubbin et al., 2012) yielded weighted average δD values of -61 ± 15‰ (95% confidence level, n = 16, MSWD = 0.61) and -125 ± 46‰ (95% confidence level, n = 5, MSWD = 0.05), consistent within errors with their bulk δD values. In a detailed study investigating IMF during H isotope analysis by SIMS, Hauri et al. (2006) have shown that IMF can vary by up to 60‰ for silicate glasses ranging in composition from basaltic to rhyolitic and containing 0.1 to 5.7 wt.% H_2O. When establishing our apatite H isotope analytical protocol using NanoSIMS at the Open University, we confirmed that using reference apatite with ~0.5 wt.% H_2O yielded accurate δD values for the Imaichi apatite that contains ~0.02 wt.% H_2O (Barnes et al., 2013; Tartèse

et al., 2013). Importantly, using apatite reference minerals to standardise merrillite volatile abundances and/or H isotope measurements is not ideal because of possible matrix effects. However, it is a common practice since there is no merrillite reference material for H_2O abundance and H isotope determination by SIMS (e.g., McCubbin et al., 2014; Mane et al., 2016; Sarafian et al., 2017b; Liu et al., 2018; Stephant et al., 2018). Both phases are Ca-rich phosphates with similar major element compositions; merrillite in GRA 06128 contains ~47 wt.% CaO and ~46 wt.% P_2O_5 (Shearer et al., 2010), compared to ~55 wt.% CaO and ~40 wt.% P_2O_5 for the apatite standards used here (McCubbin et al., 2012). In addition, GRA 06128 merrillite contains ~1.7 wt.% FeO, ~2.7 wt.% MgO and ~2.6 wt.% Na_2O (Shearer et al., 2010). A recent NanoSIMS study carried out using similar instrument conditions has shown that there is no difference in terms of calibration of H_2O abundances and of IMF for D/H ratios measured in apatite and glass matrices (Hu et al., 2015), despite these two phases having very different structures and chemical compositions. If there is no observable matrix effect between D/H ratios obtained by SIMS in apatite and glass, it is reasonable to assume that there is no significant matrix effect between the Ca phosphates apatite and merrillite. We are thus confident that standardisation of merrillite analyses using apatite standards did not adversely affect our results.

The H isotope composition of H_2O measured in apatite and merrillite are reported using the standard delta (δ) notation with respect to the D/H ratio of the Vienna Standard Mean Ocean Water (SMOW), and are corrected for background contribution of H and IMF as mentioned above. All data are reported with their 2σ uncertainties that combine the internal precision of each analysis, the reproducibility of D/H measurements on reference apatite Ap004 during the session and the uncertainty on the calculated background D/H ratio (Table 1).

2.2.2. F-Cl abundances and Cl isotope analysis

The apatite Cl isotope composition and F-Cl abundances were measured using the CAMECA NanoSIMS 50L at The University of Manchester. Analyses were carried out using a Cs^+ primary beam current of ~35 pA, with an accelerating voltage of 16 kV. Each analysis was preceded by 5 min pre-sputtering using a 250 pA primary beam rastered on the sample over 12 μm × 12 μm areas to eliminate any surface contamination. Secondary ionic species of ^{12}C, $^{16}O^1H$, ^{18}O, ^{28}Si, ^{35}Cl, ^{37}Cl, and $^{40}Ca^{19}F$ were then collected simultaneously on seven electron multipliers for 100 cycles (approximately 1 min) from the central 6 μm × 6 μm areas. An electron gun was used for charge compensation. The mass resolving power was set to ~7000 (CAMECA definition) in order to adequately resolve isobaric interferences such as ^{17}O on the $^{16}O^1H$ peak and $^{19}F^{16}O$ on the ^{35}Cl peak. Intensity of ^{12}C secondary ions was monitored to ensure that the analysed areas were free of any surficial contamination, cracks, or hotspots. The vacuum in the analysis chamber remained constant around 1.1×10^{-9} torr.

Apatite F and Cl contents were calibrated using the measured $^{40}Ca^{19}F/^{18}O$ and $^{35}Cl/^{18}O$ ionic ratios and the calibrations derived from terrestrial apatite standards (Durango apatite Ap003, Crystal Lode Pegmatite Mine apatite Ap005, and Lake Baikal apatite Ap018, all described in McCubbin et al., 2012) pressed in indium. The reported uncertainties on the F and Cl contents of GRA 06128 apatite combine the 2σ uncertainty associated with the calibration lines (±6.3% for F and ±4.6% for Cl; Fig. 2) and the analytical uncertainties associated with each individual measurement. Analysis of olivine in GRA 06128 was used to calculate F and Cl instrumental background abundances of 34.2 ± 3.8 ppm and 1.3 ± 1.6 ppm (2SD, n = 3), which were subtracted from the abundances measured in GRA 06128 apatite. Finally, the apatite Ap003 was used to correct the measured $^{37}Cl/^{35}Cl$ ratios for IMF ($\delta^{37}Cl_{SMOC}$ value of 0.3‰; e.g., Treiman et al., 2014). Cl isotopic compositions are reported using the standard δ

notation with respect to the $^{37}Cl/^{35}Cl$ ratio of the standard mean ocean chloride (SMOC). The accuracy of the $\delta^{37}Cl$ analyses was checked by repeated measurements on a second reference apatite, Ap005, which yielded a weighted average $\delta^{37}Cl$ value of 0.3 ± 1.8‰ (95% confidence level, MSWD = 1.3, n = 5; Fig. 2), consistent with a terrestrial $\delta^{37}Cl$ value near 0‰ (e.g., Sharp et al., 2013). It is important to point out that the reference apatite Ap003 used here to correct for IMF effects contains ~0.45 wt.% Cl (McCubbin et al., 2012) while Cl content of GRA 06128 apatite is about an order of magnitude higher (e.g., Shearer et al., 2011), which could have introduced a bias while correcting for IMF in these Cl-rich apatite. However, analyses carried out using the CAMECA IMS1280 ion probe indicate that IMF for Cl isotopes only differs by ~0.5‰ between Durango (Ap003) and pure Cl-apatite standards (Bellucci et al., 2017), which is much smaller than the reproducibility we obtained for $^{37}Cl/^{35}Cl$ measurements on the Ap003 reference apatite. All $\delta^{37}Cl$ values are reported with their associated 2σ uncertainties, which combine the reproducibility of $^{37}Cl/^{35}Cl$ measurements on the reference apatite Ap003 and the internal precision for each analysis.

Location of Figure 2

Finally, using the same NanoSIMS settings than for spot analysis we imaged the distribution of the secondary ionic species ^{12}C, $^{16}O^{1}H$, ^{18}O, ^{28}Si, ^{35}Cl, ^{37}Cl and $^{40}Ca^{19}F$ over a 20 μm × 20 μm area at the contact between merrillite and apatite (see location in Fig. 1C). For acquisition the 20 μm × 20 μm area was divided in 256 pixels × 256 pixels, and 150 cycles were acquired for 33 s each, resulting in a total acquisition time of ~82 minutes. Because no standard was analysed in imaging mode only raw ionic and isotope ratios are discussed.

3. Results

3.1. Water abundance and H isotope composition

Despite being a nominally anhydrous mineral, it has been reported that merrillite [$Ca_{18}Na_2Mg_2(PO_4)_{14}$] in martian shergottites can contain up to ~200 ppm H_2O (e.g., McCubbin et al., 2014). In GRA 06128, merrillite contains between ~20 and ~55 ppm H_2O (Fig. 3 and Table 1). Because of their low H_2O abundances, the D/H ratios measured in merrillite are associated with large uncertainties. Considering these uncertainties, the measured merrillite δD values appear homogeneous over the whole range of water contents, yielding a weighted average δD of -152 ± 330‰ (95% confidence level, n = 8, MSWD = 3.1, prob. = 0.003; Fig. 3).

Location of Figure 3

Apatite [$Ca_5(PO_4)_3(F,Cl,OH)$] in GRA 06128 displays a strikingly identical range of water content between ~19 and ~53 ppm H_2O (Fig. 3 and Table 1). However, D/H ratios obtained on apatite are different compared to those of merrillite, with δD values ranging between 122 ± 390‰ and 1949 ± 397‰ (Fig. 3 and Table 1). In addition, GRA 06128 apatite displays a rough inverse correlation between δD values and increasing H_2O contents (Fig. 3).

Location of Table 1

3.2. F-Cl abundances and Cl isotope composition

The NanoSIMS results obtained here confirm that apatite in GRA 06128 is Cl-rich (e.g., Shearer et al., 2011), containing 5.4-5.7 wt.% Cl and 0.6-0.8 wt.% F (Table 2). Stoichiometric calculations indicate that the GRA 06128 apatite volatile site contains 82 ± 3 mol.% Cl and 19 ± 3 mol.% F (2SD, n = 10; Table 2), and suggest almost nothing to very low

OH contents, which is consistent with the measured H_2O contents < ~50 ppm (equivalent of ~0.3 mol.% OH). The $\delta^{37}Cl$ values obtained on apatite in GRA 06128 are consistent across several grains, yielding an average $\delta^{37}Cl$ of +3.2 ± 0.7‰ (95% confidence level, n = 10, MSWD = 0.25, prob. = 0.99; Table 2). There is no correlation between F and Cl abundances and $\delta^{37}Cl$ values.

Location of Table 2

NanoSIMS imaging shows that $^{12}C/^{18}O$ and $^{16}O^{1}H/^{18}O$ ratios are roughly similar in merrillite and apatite (Fig. 4), the latter being consistent with the similar H_2O contents measured in both phosphates in spot mode. It also shows that $^{28}Si/^{18}O$, $^{35}Cl/^{18}O$, and $^{40}Ca^{19}F/^{18}O$ ratios all increase sharply at the merrillite-apatite boundary (Fig. 4).

Location of Figure 4

The Cl and Si distributions are homogeneous in apatite, while the $^{40}Ca^{19}F/^{18}O$ image seems to indicate a slight increase in F from the merrillite-apatite boundary towards the apatite interior (Fig. 4). Finally, there is little variation in the $\delta^{37}Cl$ ratio within the apatite (note that Fig. 4 displays raw $\delta^{37}Cl_{SMOC}$ not corrected for IMF, which cannot be compared with $\delta^{37}Cl$ values obtained in spot mode).

4. Discussion

4.1. Assessing the significance of the phosphate D/H ratios

At such low H_2O abundances, it is vital to ensure that the measured H_2O contents and D/H ratios have not been compromised by terrestrial contamination, either during the meteorite residence in the Antarctic ice or during sample handling and analysis in the lab.

4.1.1. Terrestrial weathering

The relationship $x \sim \sqrt{D.t}$, where x is the diffusion length scale in m, D the diffusion coefficient calculated at a given temperature, and t the time in s (e.g., Zhang, 2010), suggests that OH in apatite will diffuse over a distance of ~1.1×10^{-13} μm per billion years at 20 ºC using the diffusivity parameters for volatiles in apatite determined at 1 atm and parallel to the c-axis (Brenan, 1994). However, recent experimental work by Boyce et al. (2018) suggests that diffusion of H and D in apatite can be orders of magnitude faster. Using their diffusion parameters yields a larger diffusion length scale x of ~5.6×10^{-2} μm per billion years at 20 ºC. In any case, both sets of diffusivity parameters suggest that diffusional exchange of H isotopes between apatite and Antarctic ice would have been insignificant at low temperatures.

4.1.2. Laboratory contamination

Two processes, related to the presence of water adsorbed on the sample surface and to the presence of epoxy in cracks in the GRA 06128 polished section, can result in analytical contamination of the water contents and H isotope compositions measured in GRA 06128 phosphates. The combination of sample handling in a clean-room environment, ultra-low vacuum in the analysis chamber of the NanoSIMS 50L ion probe, pre-sputtering to clean the sample surface, and fast scanning of the large primary Cs^+ beam, all ensure that contamination due to adsorbed H sticking onto the sample surface is minimal. First, the samples curated at Johnson Space Center (Apollo and Antarctic meteorite collections) never come into contact with water during sample preparation (see details of sample preparation in

Tartèse et al., 2013). Before H isotope analyses, the GRA 06128 section was kept at 50 °C in a vacuum oven for at least a week. Just before analysis, it was coated with 30 nm thickness of gold and immediately transferred first into the airlock of the NanoSIMS where it was then kept at ~50 °C and ~1×10^{-7} torr for at least 24 hours, before being stored at ~1×10^{-9} torr in the NanoSIMS vessel storage. For analysis, the sample was transferred into the analysis chamber of the NanoSIMS in which the vacuum remained between ~3 and 5×10^{-10} torr (see methods above). Before the actual analyses, a 3 minute pre-sputtering further cleaned the sample surface. Finally, NanoSIMS analyses consisted of continuous rastering of the primary beam over 10 μm × 10 μm areas using a fast scanning rate of 0.54 s per frame, which limits redeposition of adsorbed species, together with a high primary current of 280 pA, ensuring that the proportion of water coming from the ablated materials largely dominates over contaminant water (e.g., Stephant et al., 2014; Hu et al., 2015).

The second possible source of contamination during ion probe analyses is the epoxy used to prepare the sections that naturally fills the cracks. Since the water contents measured in phosphates in GRA 06128 are very low, extreme care was taken to check for any possible contamination by epoxy, which contains large amounts of H and C. As stated in the method section, the first check consisted in monitoring in real time the secondary ion images of ^{1}H and ^{12}C during pre-sputtering of the targeted areas to ensure that they were free of any surficial contamination, cracks or hotspots. To further assess the presence of epoxy-related contamination, we also analysed the $^{12}C/^{18}O$ ratios during analyses of the phosphate water content and H isotope composition. We did not observe any correlation between the measured $^{12}C/^{18}O$ ratios and the $^{1}H/^{18}O$ and $^{2}H/^{1}H$ ratios (Fig. 5), which would be expected if the H measured in GRA 06128 phosphates comprised a mixture of H indigenous to the phosphates and originating from epoxy contamination. For comparison, these $^{12}C/^{18}O$ ratios

are lower than those measured in the indium-mounted apatite and olivine standards (8.0±0.4 × 10^{-3} for Ap004, n = 16; 1.2±0.6 × 10^{-3} for Ap005, n = 13; 13.3±0.2 × 10^{-3} for Ap018, n = 5; 2.3±0.8 × 10^{-3} for Ap020, n = 13; 0.9±0.3 × 10^{-3} for San Carlos olivine, n = 16), and more than six orders of magnitude lower compared to the $^{12}C/^{18}O$ ratio of ~2.9±0.1 × 10^{3} (n = 5) measured in the epoxy with which GRA 06128 has been prepared.

Location of Figure 5

4.1.3. Cosmic-ray spallation

D/H ratios can also be modified and driven toward D enrichment in response to spallation reactions, induced by exposure to cosmic and galactic cosmic rays in materials residing within the upper ~2-3 m of planetary bodies and during transfer of meteorites to the Earth (e.g., Williams and Gold, 1975), especially in minerals with low H_2O contents (e.g., Füri et al., 2017). Taking the cosmic-ray exposure age of ~3 Ma obtained by Lindsay et al. (2014), and using the lunar production rate of spallogenic D (~2.2 × 10^{-12} mol g^{-1} Ma^{-1}; Füri et al., 2017), which represents an upper limit since the abundance of target elements such as O, Mg, Al, Si, and Fe from which spallogenic D is produced is lower in apatite and merrillite compared to olivine, correction for spallation effects results in a negligible maximal correction of δD values by ~20‰ for an H_2O content of 20 ppm. This is well within uncertainties associated with the measured δD values (Fig. 3), indicating that spallation effects have had a negligible impact on the D/H ratios measured in GRA 06128 phosphates.

4.2. Water abundance and H isotope composition of GRA 06128 partial melts

Since experimental constraints on partitioning of water between merrillite and silicate melts do not exist, we cannot precisely estimate the water content of the melt from which GRA

06128 merrillite crystallised. It should be noted that the widespread presence of nominally anhydrous merrillite as the magmatic phosphate, rather than apatite, does not necessarily imply that the GRA 06128 melts were depleted in water. Indeed, the stability of merrillite versus apatite is likely more dependent on the P to halogen ratio rather than on the melt water content, since merrillite with up to *ca*. 200 ppm H_2O has been observed in a martian shergottite whose residual melt contained ~1.5 to 3.0 wt.% H_2O at the time of phosphate crystallisation (McCubbin et al. 2014). Experimental constraints obtained on water partitioning between other nominally anhydrous minerals and silicate melts can be used to get a qualitative estimate of the GRA 06128/9 melt H_2O abundance at the time of merrillite crystallisation. Merrillite H_2O contents of 20 to 55 ppm would correspond to melt H_2O abundances of *ca*. 400-2000 to 1000-5500 ppm using $D^{pyroxene/melt}$ (~0.01-0.05; see McCubbin et al., 2015b and references therein). Using $D^{olivine/melt}$ (~0.0010-0.0025; see McCubbin et al., 2015b and references therein) the calculated melt H_2O abundances increase to *ca*. 0.8-2.0 wt.% up to 2.2-5.5 wt.%. Once again, although the lack of experimental constraints on water partitioning between merrillite and silicate melts prevents us to provide robust estimates for the GRA 06128/9 melt H_2O abundance, it is still important to point out that the moderate merrillite H_2O contents could still be consistent with relatively water-rich partial melts.

Magmatic merrillite yielded an average δD value of -152 ± 330‰. Once again there is no experimental data on H isotope fractionation between merrillite and melt, preventing us to directly estimate the D/H ratio of the melt from which merrillite formed. A compilation of δD values obtained on nominally anhydrous minerals from samples derived from the Earth mantle indicates that their δD values can be up to ~50‰ lower compared to their mantle source (e.g., Bell and Ihinger, 2000). Such magnitude of H isotope fractionation is small compared to the uncertainty associated with the mean merrillite δD value determined here.

Therefore, the measured δD values of the merrilite likely provides a good first order approximation for the indigenous, magmatic, D/H ratio of water present in the felsic melts from which GRA 06128 merrillite crystallised.

This does not necessarily indicate that merrillite has recorded the original D/H ratio of the GRA 06128 partial melts since magmatic degassing of volatile species such as H_2 can lead to large H isotope fractionation, as shown for lunar mare basalts, for example (Tartèse and Anand, 2013; Tartèse et al., 2013, 2014b). Together with pressure and the abundance of dissolved H species in a melt, oxygen fugacity (fO_2) is a primary parameter controlling the speciation of H between H_2, H_2O and OH species dissolved in a melt (e.g., Hirschmann et al., 2012). At low fO_2 typical for mare basalts of around IW-1 (Whadwa, 2008), H_2 largely dominates over H_2O in the gas phase (e.g., Tartèse et al., 2013). However, the fO_2 during crystallisation of GRA 06128/9 is estimated to be higher, between IW+0.5 and IW+1.5 (Shearer et al., 2010). Calculation using the CHO software (https://www.esc.cam.ac.uk/research/research-groups/research-projects/tim-hollands-software-pages/cho) suggests that at 1 bar and 1100 ºC, the conditions at which GRA 06128/9 melts could have crystallised (e.g., Lunning et al., 2017), a degassed vapour phase would be dominated by H_2O over H_2 at fO_2 > IW+0.2, with $X(H_2O)$ ~ 0.7 and $X(H_2)$ ~ 0.3 at IW+1, for example. D/H fractionation associated with vapour degassing at such H_2O/H_2 mixing ratio, which is similar to estimates made by Sarafian et al. (2017) for the angrite parent body, is limited to a few tens of permil for up to 80-90% of H-bearing species lost. It is thus unlikely that the D/H ratio of H_2O/OH dissolved in GRA 06128/9 melts dramatically increased during their crystallisation in response to degassing of H-bearing species, and we consider that the merrillite average δD value of -152 ± 330‰ provides a good estimate for the δD value of primordial H trapped in the GRA 06128/9 parent body.

4.3. Halogen inventory of apatite-forming fluids in GRA 06128

Our results confirm that apatite in GRA 06128/9 is Cl-rich and OH-poor, suggesting that it formed via replacement reactions of merrillite during interaction with Cl-rich fluids (e.g., Shearer et al., 2011). Precisely quantifying the F, Cl and OH contents of the fluid from which apatite formed is not straightforward, however, since these elements are major constituents in the apatite structure, implying that their partitioning between apatite and melt or fluid does not follow Henry's law (e.g., Boyce et al., 2014; McCubbin et al., 2015a). All experimental results indicate that F is strongly compatible in the apatite structure, with $D_F^{\text{ap-fluid}}$ ranging between ~70 and 300 depending on the F abundance in the fluid phase (e.g., Kusebauch et al., 2015a,b and references therein). The F abundance measured in GRA 06128 apatite (0.62-0.82 wt.% F) thus only requires a fluid with ~20-120 ppm F. Cl partitioning between apatite and fluids is more complex, with experimental $D_{Cl}^{\text{ap-fluid}}$ values ranging between ~0.1 to 2 and varying with many parameters such as temperature, pressure, pH, and the amount and composition of the fluid (e.g., Mathez and Webster, 2005; Doherty et al., 2014; Kusebauch et al., 2015a,b; Webster et al., 2017). Using this range of $D_{Cl}^{\text{ap-fluid}}$ values suggests that the fluid from which GRA 06128 formed might have contained from ~3 wt.% up to 56 wt.% Cl, a range comparable to that of oceanic hydrothermal fluids (e.g., Nehlig, 1991) or evaporated seawater brines in continental basins on Earth, for example (e.g., Richard et al., 2011). Interestingly, formation of near Cl-apatite end-member, similar in composition to GRA 06128 apatite, from Cl-rich brine-type fluids has been reported in some terrestrial settings such as the Bamble sector in southeast Norway (e.g., Engvik et al., 2009, 2011; Kusebauch et al., 2015a).

4.4. H and Cl isotope composition of apatite-forming fluids in GRA 06128

The average δ^{37}Cl value of +3.2 ± 0.7‰ obtained here on GRA 06128 apatite is higher than the δ^{37}Cl value of +1.2‰ obtained on a bulk GRA 06129 leachate by Shearer et al. (2011) (Fig. 6). However, the Cl content of 66 ppm Cl reported for the GRA 06129 leachate by Shearer et al. (2011) may hint at incomplete leaching of Cl from apatite. Indeed, considering that all the Cl in GRA 06128/9 is hosted in chlorapatite, and based on the reported apatite modal abundance of ~0.5 to 1.8% for GRA 06128/9 (Day et al., 2009, 2012; Shearer et al., 2010) and an average apatite Cl content of 5 wt.%, the bulk Cl content of GRA 06128/9 should be around 250-900 ppm, which is significantly higher than the 66 ppm Cl reported for the GRA 06129 leachate. An incomplete extraction of Cl during leaching, which could have been accompanied by selective leaching and/or Cl isotope fractionation, could thus explain the discrepancy between the δ^{37}Cl values we obtained *in situ* on apatite and the bulk leachate δ^{37}Cl value reported by Shearer et al. (2011). In addition, leaching of a bulk GRA 06129 sample may have dissolved Cl-bearing terrestrial components possibly present in cracks, which would likely decrease the original δ^{37}Cl value since most terrestrial reservoirs have a δ^{37}Cl value around 0‰ (Sharp et al., 2013). The δ^{37}Cl values obtained *in situ* on apatite using NanoSIMS are also slightly higher than the two ion probe apatite δ^{37}Cl values reported by Shearer et al. (2011) (Fig. 6). The cause(s) for this discrepancy is unclear but it may indicate a small variability of δ^{37}Cl values in GRA 06128/9 apatite that the limited number of grains we targeted did not reveal. Apatite F and Cl abundances reported by Shearer et al. (2011), Day et al. (2012) and Zhou et al. (2018) are more variable than those we measured in the three phosphate assemblages we studied, for example.

Location of Figure 6

It has been shown experimentally that Rayleigh distillation of $HCl_{(g)}$ from hydrochloric acid solutions can induce large Cl isotope fractionation, either negative or positive depending notably on the acidity of the starting solution (Sharp et al., 2010a; Rodriguez et al., 2018). Distillation of $HCl_{(g)}$ from strongly acidic hydrochloric acids causes large ^{37}Cl enrichment of Cl remaining in the fluids due to preferential loss of ^{35}Cl in the vapour phase (Sharp et al., 2010a; Rodriguez et al., 2018), while $HCl_{(g)}$ distilled from diluted hydrochloric acid solutions is preferentially enriched in ^{37}Cl, leaving behind a residue enriched in ^{35}Cl (Sharp et al., 2010a; Rodriguez et al., 2018). In GRA 06128/9, apatite composition is consistent with formation through interaction of Cl-rich acidic fluids with merrillite at temperatures probably around 600-800 ºC (e.g., Shearer et al., 2011). There is no experimental data on Cl isotope fractionation between apatite and fluids, but it is likely to be small at sub-solidus temperatures, so we assume here that the apatite Cl isotope composition corresponds to that of the fluid from which it formed. In this case, results from experimental studies involving highly concentrated hydrochloric acids suggest that residual $\delta^{37}Cl$ values of *ca.* +3‰ would be achieved after the fluid phase had lost ~50% of its initial Cl content through Rayleigh distillation, starting from a 'chondritic' $\delta^{37}Cl$ value of 0‰ (Sharp et al., 2010a; Rodriguez et al., 2018). Alternatively, distillation of $HCl_{(g)}$ from diluted hydrochloric acid solutions would result in vapour $\delta^{37}Cl$ values of *ca.* +3‰ after the fluid phase had lost ~60-70% of its initial Cl content, again starting from a 'chondritic' $\delta^{37}Cl$ value of 0‰ (Sharp et al., 2010a). Both mechanisms may thus explain the Cl isotope composition measured in GRA 06128 apatite. However, temperatures above ~500-600 ºC estimated for formation of GRA 06128/9 apatite (e.g., Shearer et al., 2011) suggest it formed through merrillite interaction with fumarole-like fluids from which most H_2O would have been driven off instead of aqueous fluids, favouring the diluted hydrochloric acid formation scenario.

The δD values measured *in situ* on GRA 06128 apatite range between *ca*. 120‰ and 1950‰ and show an inverse correlation with apatite H_2O abundance (Fig. 3). This is in contrast with the merrillite δD values that appear homogeneous around -150 ± 300‰ across the range of H_2O abundances. Interestingly, H_2O abundance in co-existing merrillite and apatite are similar to each other (~21-24 ppm in Mer#1 and 20-32 ppm in Ap#1, ~23-30 ppm in Mer#2 and 25-31 ppm in Ap#2, and ~51-56 ppm in Mer#3 and 53-54 ppm in Ap#3; Table 1), indicating that only minute amounts of H were brought in during the transformation of merrillite into apatite, if any. In the phosphate assemblage #3 that contains the highest H_2O abundance, the merrillite and apatite δD values are similar within error, while in the phosphate assemblage #2 with the lowest H_2O abundance, the apatite δD values are *ca*. 2000‰ higher than those of merrillite (Fig. 3). H loss from apatite via diffusion is an appealing mechanism to explain the inverse correlation between δD values and H_2O abundances for apatite. However, the observed δD increase associated with H_2O abundance decrease is several hundreds of permil higher than that predicted by H loss via diffusion (Fig. 7), calculated using a Rayleigh distillation equation and the most favourable case where the species lost through diffusion are protons and deuterons (e.g., using a α fractionation factor equal to $\sqrt{(m_D/m_H)}$; see Rosckosz et al., 2018). The only viable mechanism that could explain these observations is associated with metasomatic alteration of merrillite accompanied by the introduction of traces amount of H into newly-formed apatite from fumarole-like fluids with elevated D/H ratios. Modelling calculations show that adding 2 to 10 ppm H_2O with δD values between 15000‰ and 4000‰, respectively, to phosphate initially containing *ca*. 20-80 ppm H_2O reproduces fairly well the range of D/H ratios and H_2O contents measured in GRA 06128 apatite (Fig. 7).

Location of Figure 7

4.5. Origin of the apatite-forming fluids in GRA 06128/9

GRA 06128/9 apatite formed *ca*. 100 Ma after parent body accretion and partial melting (e.g., Shearer et al., 2011; Zhou et al., 2018) from interaction of magmatic merrillite with metasomatic fluids at sub-solidus temperatures. Metamorphism due to internal heating on asteroidal parent bodies typically occurs within ~60 Ma after the formation of CAIs (e.g., Göpel et al. 1994). Therefore, the only viable heat source to drive fluid circulations at such a late stage is likely related to impact processes. Metasomatic fluids could have been derived from the GRA 06128/9 parent body and/or from the impactor. As detailed above, these apatite-forming fluids were highly enriched in Cl. Also, H isotope systematics suggests that the minute amounts of H introduced in the Cl-apatite were likely characterised by δD values > 3000-4000‰. At this stage it is difficult to assess whether these fluids had elevated D/H ratios to start with, or if elevated fluid D/H ratios resulted from processes related to H_2 fractionation from water associated with radiolysis or with open system metal and sulphides reduction (e.g., Alexander et al., 2010). The late-stage formation of apatite suggests that water dissociation via radiolysis is unlikely since short lived isotopes such as ^{26}Al or ^{60}Fe would have already decayed away. Extreme H isotope fractionation due to reduction of metal and/or sulphides is also unlikely since the magnitude of H isotopic fractionation between H_2 and H_2O does not exceed ~300‰ at temperatures > 500 ºC (e.g., Bottinga, 1969). D/H fractionation may have also occurred in response to continuous distillation of HCl-rich fluids. As far as we are aware there are no experimental constraints on H isotope fractionation during HCl distillation, but such a process is unlikely to shift δD values by thousands of permil at sub-solidus temperatures. Apatite-forming fluids may thus have been characterised by elevated D/H ratios to start with. Very few Solar System water reservoirs have δD values around 3000-4000‰ or above. They include phyllosilicates in the matrix of the primitive

Semarkona LL3.00 ordinary chondrite, with δD values up to *ca.* 10000‰ (e.g., Piani et al., 2015), and H-bearing minerals in the LaPaz Icefield 04840 R chondrite, with δD values of ~2700-3700‰ (McCanta et al., 2008). D/H ratios of cometary water appear to be slightly lower, with δD values up to ~2400 ± 500‰ for comet 67P/Churyumov-Gerasimenko (Altwegg et al., 2015). Based on all these observations, a plausible scenario is envisaged in which apatite in GRA 06128/9 formed from fumarole-like fluids, at the expense of magmatic merrillite. These fluids may have been derived from D- and HCl-rich ices condensed in the outer Solar System at temperatures around 150 K (e.g., Zolotov and Mirnonenko, 2007), which could have been delivered to the GRA 06128/9 parent-body by an ice-rich impactor. Further heating driven by the impact event would have resulted in ice sublimation, allowing percolation of hot Cl-rich 'briny' fumaroles in the crustal regions of the GRA 06128/9 parent body.

5. Implications

There is a strong similarity between merrillite-apatite assemblages in GRA 06128/9 and those observed in ordinary chondrites (e.g., Jones et al., 2014, 2016; Lewis and Jones, 2016). Apatite in ordinary chondrites is also generally OH-poor and Cl-rich and thought to have formed from metasomatic reactions between pre-existing merrillite and Cl-rich fluids. Fluid circulations and metasomatism on asteroidal bodies occurring several tens of million years after their accretion thus seem to be fairly common in Solar System objects.

GRA 06128/9 is thought to have crystallised from a felsic melt formed through low- to moderate degrees (< 30%) of partial melting of a volatile-rich chondritic precursor possibly similar to R chondrites, leaving a residuum with brachinite-like compositions (e.g., Day et al., 2009, 2012; Gardner-Vandy et al., 2013; Wang et al., 2014; Lunning et al., 2017). On the

other hand, O isotope characteristics of GRA 06128/9 and the brachinite meteorites ($\delta^{18}O$ = *ca*. 4-5 ‰ and $\Delta^{17}O$ = -0.25 ± 0.15 ‰) preclude any direct relationships with any of the known groups of chondritic meteorites (Day et al., 2012; Greenwood et al., 2012). The isotopic composition of indigenous H in GRA 06128/9 is broadly consistent with that estimated for indigenous H in other asteroidal and planetary bodies such as the angrite and HED parent bodies, Mars, and the Moon (Hallis et al., 2012; Usui et al., 2012; Saal et al., 2013; Tartèse and Anand, 2013; Tartèse et al., 2013, 2014b; Barnes et al., 2014; Sarafian et al., 2014, 2017a, 2017b; Barrett et al., 2016), and with the bulk D/H ratios measured in water-rich carbonaceous chondrites such as CM and CI chondrites (e.g., Alexander et al. 2012). All these results are consistent with early accretion of locally-derived volatiles on the asteroidal parent bodies of GRA 06128/9, the angrites, and the HED meteorites within a few millions years after the formation of the Solar System (e.g., Misawa et al., 2005; Shearer et al., 2010; Zhou et al., 2013, Sarafian et al., 2017a).

Acknowledgments

We are grateful to the NASA Meteorite Working Group for allocation of GRA 06128 samples, and to I.C. Lyon for his help in the NanoSIMS lab in Manchester. This research was supported by UK Science and Technology Facilities Council (STFC) research grants (ST/I001298/1 to M.A. and ST/P005225/1 to R.T.) and by the UK Cosmochemical Analysis Network (UKCAN, grant ST/I001964/1 to I.A.F.) for NanoSIMS machine time allocation at the Open University. At The University of Manchester, the NanoSIMS was funded by UK Research Partnership Investment Funding (UKRPIF) Manchester RPIF Round 2. We thank Adam Sarafian and two anonymous referees for their thorough and insightful reviews. Finally, MA would like to dedicate this manuscript to the memory of Larry Taylor for sharing his uninhibited enthusiasm and energy for research.

References

Abernethy F. A. J., Verchovsky A. B., Starkey N. A., Anand M., Franchi I. A. and Grady M. M. (2013) Stable isotope analysis of carbon and nitrogen in angrites. *Meteorit. Planet. Sci.* **48**, 1590-1606.

Albarède F. (2009) Volatile accretion history of the terrestrial planets and dynamic implications. *Nature* **461**, 1227-1233.

Alexander C. M. O'D., Newsome S. D., Fogel M. L., Nittler L. R., Busemann H. and Cody G. D. (2010) Deuterium enrichments in chondritic macromolecular material–implications for the origin and evolution of organics, water and asteroids. *Geochim. Cosmochim. Acta* **74**, 4417-4437.

Alexander C. M. O.'D., Bowden R., Fogel M. L., Howard K. T., Herd C. D. K. and Nittler L. R. (2012) The provenances of asteroids, and their contributions to the volatile inventories of the terrestrial planets. *Science* **337**, 721-723.

Altwegg K., Balsiger H., Bar-Nun A., Berthelier J. J., Bieler A., Bochsler P., Briois C., Calmonte U., Combi M., De Keyser J., Eberhardt P., Fiethe B., Fuselier S., Gasc S., Gombosi T. I., Hansen K. C., Hässig M., Jäckel A., Kopp E., Korth A., LeRoy L., Mall U., Marty B., Mousis O., Neefs E., Owen T., Rème H., Rubin M., Sémon T., Tzou C. Y., Waite H. and Wurz P. (2015) 67P/Churyumov-Gerasimenko, a Jupiter family comet with a high D/H ratio. *Science* **347**, 1261952-1.

Aubaud C., Withers A. C., Hirschmann M. M., Guan Y., Leshin L. A., Mackwell S. J. and Bell D. R. (2007) Intercalibration of FTIR and SIMS for hydrogen measurements in glasses and nominally anhydrous minerals. *Am. Mineral.* **92**, 811-828.

Barnes J. D., Sharp Z. D. and Fischer T. P. (2009) Variations in chlorine stable isotopes along the Central American volcanic front. *Geochem. Geophys. Geosyst.* **10**, doi: 10.1029/2009GC002587

Barnes J. J., Franchi I. A., Anand M., Tartèse R., Starkey N. A., Koike M., Sano Y. and Russell S. S. (2013) Accurate and precise measurements of the D/H ratio and hydroxyl content in lunar apatites using NanoSIMS. *Chem. Geol.* **337-338**, 48-55.

Barnes J. J., Tartèse R., Anand M., McCubbin F. M., Franchi I. A., Starkey N. A. and Russell S. S. (2014) The origin of water in the primitive Moon as revealed by the lunar highlands samples. *Earth Planet. Sci. Lett.* **390**, 244-252.

Barnes J. J., Tartèse R., Anand M., McCubbin F. M., Neal C. R. and Franchi I. A. (2016) Early degassing of lunar urKREEP by crust-breaching impact(s). *Earth Planet. Sci. Lett.* **447**, 84-94.

Barrat J. A., Sansjofre P., Yamaguchi A., Greenwood R. C. and Gillet P. (2017) Carbon isotopic variation in ureilites: Evidence for an early, volatile-rich Inner Solar System. *Earth Planet. Sci. Lett.* **478**, 143-149.

Barrett T. J., Barnes J. J., Tartèse R., Anand M., Franchi I. A., Greenwood R. C., Charlier B. L. A. and Grady M. M. (2016) The abundance and isotopic composition of water in eucrites. *Meteorit. Planet. Sci.* **51**, 1110-1124.

Bell D. R. and Ihinger P. D. (2000) The isotopic composition of hydrogen in nominally anhydrous mantle minerals. *Geochim. Cosmochim. Acta* **64**, 2109-2118.

Bellucci J. J., Whitehouse M. J., John T., Nemchin A. A., Snape J. F., Bland P. A. and Benedix G. K. (2017) Halogen and Cl isotopic systematics in Martian phosphates: Implications for the Cl cycle and surface halogen reservoirs on Mars. *Earth Planet. Sci. Lett.* **458**, 192-202.

Bottinga Y. (1969) Calculated fractionation factors for carbon and hydrogen isotope exchange in the system calcite-carbon dioxide-graphite-methane-hydrogen-water vapor. *Geochim. Cosmochim. Acta* **33**, 49-64.

Boyce J. W., Tomlinson S. M., McCubbin F. M., Greenwood J. P. and Treiman A. H. (2014) The lunar apatite paradox. *Science* **344**, 400-402.

Boyce J. W., Treiman A. H., Guan Y., Ma C., Eiler J. M., Gross, J., Greenwood J. P. and Stolper E. M. (2015) The chlorine isotope fingerprint of the lunar magma ocean. *Science Advances* **1**, e1500380.

Boyce J. W., Baker M. B., Guan Y. and Macris C. A. (2018) Hydrogen diffusion in apatite. *Lunar Planet. Sci. XLIX*. Lunar Planet. Inst., Houston. #2492 (abstr.).

Brenan J. (1994) Kinetics of fluorine, chlorine and hydroxyl exchange in fluorapatite. *Chem. Geol*. **110**, 195-210.

Claydon J. L., Crowther S. A., Fernandes V. A. and Gilmour J. D. (2015) Noble gases and halogens in Graves Nunataks 06129: The complex thermal history of a felsic asteroid crust. *Geochim. Cosmochim. Acta* **159**, 177-189.

Day J. M. D., Ash R. D., Liu Y., Bellucci J. J., Rumble D., McDonough W. F., Walker R. J. and Taylor L. A. (2009) Early formation of evolved asteroidal crust. *Nature* **457**, 179-182.

Day J. M. D., Walker R. J., Ash R. D., Liu Y., Rumble D., Irving A. J., Goodrich C. A., Tait K., McDonough W. F. and Taylor L. A. (2012) Origin of felsic achondrites Graves Nunataks 06128 and 06129, and ultramafic brachinites and brachinite-like achondrites by partial melting of volatile-rich primitive parent bodies. *Geochim. Cosmochim. Acta* **81**, 94-128.

Doherty A., Webster J. D. Goldoff B. and Piccoli P. (2014) Partitioning behaviour of chlorine and fluorine in felsic melt–fluid(s)–apatite systems at 50 MPa and 850–950 °C. *Chem. Geol.* **384**, 94-111.

Downes H., Abernethy F. A. J., Smith C. L., Ross A. J., Verchovsky A. B., Grady M. M., Jenniskens P. and Shaddad M. H. (2015) Isotopic composition of carbon and nitrogen in ureilitic fragments of the Almahata Sitta meteorite. *Meteorit. Planet. Sci.* **50**, 255-272.

Engvik A. K, Golla-Schindler U., Berndt J., Austrheim H. and Putnis A. (2009) Intragranular replacement of chlorapatite by hydroxy-fluor-apatite during metasomatism. *Lithos* **112**, 236-246.

Engvik A. K., Mezger K., Wortelkamp S., Bast R., Corfu F., Korneliussen A., Ihlen P., Bingen B. and Austrheim H. (2011) Metasomatism of gabbro-mineral replacement and element mobilization during the Sveconorwegian metamorphic event. *J. Metamorph. Geol*. **29**, 399-423.

Füri E., Deloule D. and Trappitsch R. (2017) The production rate of cosmogenic deuterium at the Moon's surface. *Earth Planet. Sci. Lett.* **474**, 76-82.

Gardner-Vandy K. G., Lauretta D. S. and McCoy T. J. (2013) A petrologic, thermodynamic and experimental study of brachinites: Partial melt residues of an R chondrite-like precursor. *Geochim. Cosmochim. Acta* **122**, 36-57.

Göpel C., Manhès G. and Allègre C. J. (1994) U-Pb systematics of phosphates from equilibrated ordinary chondrites. *Earth Planet. Sci. Lett.* **121**, 153-171.

Grady M. M. and Wright I. P. (2003) The abundance and isotopic composition of carbon and nitrogen in meteorites. In *Solar system history from isotopic signatures of volatile elements* (eds. R. Kallenbach, T. Encrenaz, J. Geiss, K. Mauersberger, T. Owen and F. Robert). Kluwer Academic Publishers, Dordrecht. pp. 231-248.

Grady M. M., Wright I. P., Swart P. K. and Pillinger C. T. (1985) The carbon and nitrogen isotopic composition of ureilites: implications for their genesis. *Geochim. Cosmochim. Acta* **49**, 903-915.

Grady M. M., Wright I. P. and Pillinger C. T. (1997) Carbon in howardite, eucrite and diogenite basaltic achondrites. *Meteorit. Planet. Sci.* **32**, 863-868.

Greenwood R. C., Franchi I. A., Jambon A. and Buchanan P. C. (2005) Widespread magma oceans on asteroidal bodies in the early Solar System. *Nature* **435**, 916-918.

Greenwood R. C., Franchi I. A., Gibson J. M. and Benedix G. K. (2012) Oxygen isotope variation in primitive achondrites: The influence of primordial, asteroidal and terrestrial processes. *Geochim. Cosmochim. Acta* **94**, 146-163.

Halliday A. N. (2013) The origins of volatiles in the terrestrial planets. *Geochim. Cosmochim. Acta* **105**, 146-171.

Hallis L. J., Taylor G. J., Nagashima K. and Huss G. R. (2012) Magmatic water in the martian meteorite Nakhla. *Earth Planet. Sci. Lett.* **359-360**, 84-92.

Hauri E. H., Shaw A. M., Wang J., Dixon J. E., King P. L. and Mandeville C. (2006) Matrix effects in hydrogen isotope analysis of silicate glasses by SIMS. *Chem. Geol.* **235**, 352-365.

Hirschmann M. M., Withers A. C., Ardia P. and Foley N. T. (2012) Solubility of molecular hydrogen in silicate melts and consequences for volatile evolution of terrestrial planets. *Earth Planet. Sci. Lett.* **345-348**, 38-48.

Hu S., Lin Y., Zhang J., Hao J., Yang W. and Deng L. (2015) Measurements of water content and D/H ratio in apatite and silicate glasses using NanoSIMS 50L. *J. Anal. Atom. Spectrom.* **30**, 967-978.

John T., Layne G. D., Haase K. M. and Barnes J. D. (2010) Chlorine isotope evidence for crustal recycling into the Earth's mantle. *Earth Planet. Sci. Lett.* **298**, 175-182.

Jones R. H., McCubbin F. M., Dreeland L., Guan Y., Burger P. V. and Shearer C. K. (2014) Phosphate minerals in LL chondrites: A record of the action of fluids during metamorphism on ordinary chondrite parent bodies. *Geochim. Cosmochim. Acta* **132**, 120-140.

Jones R. H., McCubbin F. M. and Guan Y. (2016) Phosphate minerals in the H group of ordinary chondrites, and fluid activity recorded by apatite heterogeneity in the Zag H3-6 regolith breccia. *Am. Mineral.* **101**, 2452-2467.

Kusebauch C., John T., Whitehouse M. J. and Engvik A. K. (2015a) Apatite as probe for the halogen composition of metamorphic fluids (Bamble Sector, SE Norway). *Contrib. Mineral. Petrol.* **170**, 34, doi: 10.1007/s00410-015-1188-6.

Kusebauch C., John T., Whitehouse M. J., Klemme S. and Putnis A. (2015b) Distribution of halogens between fluid and apatite during fluid-mediated replacement processes. *Geochim. Cosmochim. Acta* **170**, 225-246.

LaTourrette T. and Wasserburg G. J. (1998) Mg diffusion in anorthite: implications for the formation of early solar system planetesimals. *Earth Planet. Sci. Lett.* **158**, 91-108.

Lécuyer C., Gillet P. and Robert F. (1998) The hydrogen isotope composition of seawater and the global water cycle. *Chem. Geol*. **145**, 249-261.

Lee T., Papanastassiou D. A. and Wasserburg G. J. (1976) Demonstration of ^{26}Mg excess in Allende and evidence for ^{26}Al. *Geophys. Res. Lett.* **3**, 41-44.

Lewis J. A. and Jones R. H. (2016) Phosphate and feldspar mineralogy of equilibrated L chondrites: The record of metasomatism during metamorphism in ordinary chondrite parent bodies. *Meteorit. Planet. Sci*. **51**, 1886-1913.

Lindsay F. N., Herzog G. F., Park J., Delaney J. S., Turrin B. D. and Swisher III C. C. (2014) ^{40}Ar/^{39}Ar dating of microgram feldspar grains from the paired feldspathic achondrites GRA 06128 and 06129. *Geochim. Cosmochim. Acta* **129**, 96-110.

Liu Y., Chen Y., Guan Y., Ma C., Rossman G. R., Eiler J. M. and Zhang Y. (2018) Impact-melt hygrometer for Mars: The case of shergottite Elephant Moraine (EETA) 79001. *Earth Planet. Sci. Lett.* **490**, 206-215.

Lunning N. G., Gardner-Vandy K. G., Sosa E. S., McCoy T. J., Bullock E. S. and Corrigan C. M. (2017) Partial melting of oxidized planetesimals: An experimental study to test the formation of oligoclase-rich achondrites Graves Nunataks 06128 and 06129. *Geochim. Cosmochim. Acta* **214**, 73-85.

Mane P., Hervig R., Wadhwa M., Garvie L. A. J., Balta J. B. and McSween Jr H. Y. (2016) Hydrogen isotopic composition of the Martian mantle inferred from the newest Martian meteorite fall, Tissint. *Meteorit. Planet. Sci.* **51**, 2073-2091.

Marty B. (2012) The origins and concentrations of water, carbon, nitrogen and noble gases on Earth. *Earth Planet. Sci. Lett.* **313-314**, 56-66.

Mathez E. A. and Webster J. D. (2005) Partitioning behavior of chlorine and fluorine in the system apatite-silicate melt-fluid. *Geochim. Cosmochim. Acta* **69**, 1275-1286.

McCanta M. C., Treiman A H., Dyar M. D., Alexander C. M. O'D., Rumble III D. and Essene E. J. (2008) The LaPaz Icefield 04840 meteorite: mineralogy, metamorphism, and origin of an amphibole- and biotite-bearing R chondrite. *Geochim. Cosmochim. Acta* **72**, 5757-5780.

McCord T. B., Adams J. B. and Johnson T. V. (1970) Asteroid Vesta: Spectral reflectivity and compositional implications. *Science* **168**, 1445-1447.

McCubbin F. M., Hauri E. H., Elardo S. M., Vander Kaaden K. E., Wang J. and Shearer C. K. (2012) Hydrous melting of the martian mantle produced both enriched and depleted shergottites. *Geology* **40**, 683-686.

McCubbin F. M., Shearer C. K., Burger P. V., Hauri E. H., Wang J., Elardo S. M. and Papike J. J. (2014) Volatile abundances of coexisting merrillite and apatite in the martian meteorite Shergotty: Implications for merrillite in hydrous magmas. *Am. Mineral*. **99**, 1347-1354.

McCubbin F. M., Vander Kaaden K. E., Tartèse R., Boyce J. W., Mikhail S., Whitson E. S., Bell A. S., Anand M., Franchi I. A., Wang J. and Hauri E. H. (2015a) Experimental

investigation of F, Cl, and OH partitioning between apatite and Fe-rich basaltic melt at 1.0-1.2 GPa and 950-1000 °C. *Am. Mineral*. **100**, 1790-1802.

McCubbin F. M., Vander Kaaden K. E., Tartèse R., Klima, R.L., Liu, Y., Mortimer, J., Barnes, J.J., Shearer, C.K., Treiman, A.H., Lawrence, D.J., Elardo, S.M., Hurley, D.M., Boyce J. W. and Anand M. (2015b) Magmatic volatiles (H, C, N, F, S, Cl) in the lunar mantle, crust, and regolith: Abundances, distributions, processes, and reservoirs. *Am. Mineral*. **100**, 1668-1707.

Misawa K., Yamaguchi A. and Hiroshi K. (2005) U-Pb and ^{207}Pb-^{206}Pb ages of zircons from basaltic eucrites: Implications for early basaltic volcanism on the eucrite parent body. *Geochim. Cosmochim. Acta* **69**, 5847-5861.

Miura Y. and Sugiura N. (1993) Nitrogen isotopic compositions in three Antarctic and two non-Antarctic eucrites. *NIPR Symposium on Antarctic Meteorites VI*, pp. 338-356.

Nehlig P. (1991) Salinity of oceanic hydrothermal fluids: a fluid inclusion study. *Earth Planet. Sci. Lett*. **102**, 310-325.

Piani L., Robert F. and Remusat L. (2015) Micron-scale D/H heterogeneity in chondrite matrices: A signature of the pristine solar system water? *Earth Planet. Sci. Lett*. **415**, 154-164.

Pontoppidan K. M., Salyk C., Bergin E. A., Brittain S., Marty B., Mousis O. and Öberg K. L. (2014) Volatiles in Protoplanetary Disks. In *Protostars and Planets VI* (eds. H. Beuther, R. Klessen, C. Dullemond and T. Henning). Univ. Arizona Press, Tucson. pp. 363-386.

Potts N. J., Barnes J. J., Tartèse R., Franchi I. A. and Anand M. (2018) Chlorine isotopic compositions of apatite in Apollo 14 rocks: Evidence for widespread vapor-phase metasomatism on the lunar nearside ~4 billion years ago. *Geochim. Cosmochim. Acta* **230**, 46-59.

Rai V. K., Murty S. V. S. and Ott U. (2003) Nitrogen components in ureilites. *Geochim. Cosmochim. Acta* **60**, 2213-2237.

Richard A., Banks D. A., Mercadier J., Boiron M. C., Cuney M. and Cathelineau M. (2011) An evaporated seawater origin for the ore-forming brines in unconformity-related uranium deposits (Athabasca Basin, Canada): Cl/Br and δ^{37}Cl analysis of fluid inclusions. *Geochim. Cosmochim. Acta* **75**, 2792-2810.

Rodriguez A., van Bergen M. J. and Eggenkamp H. G. M. (2018) Experimental evaporation of hyperacid brines: Effects on chemical composition and chlorine isotope fractionation. *Geochim. Cosmochim. Acta* **222**, 467-484.

Roskosz M., Deloule E., Ingrin J., Depecker C., Laporte D., Merkel S., Remusat L. and Leroux H. (2018) Kinetic D/H fractionation during hydration and dehydration of silicate glasses, melts and nominally anhydrous minerals. *Geochim. Cosmochim. Acta* **233**, 14-32.Saal A. E., Hauri E. H., Van Orman J. A. and Rutherford M. J. (2013) Hydrogen isotopes in lunar volcanic glasses and melt inclusions reveal a carbonaceous chondrite heritage. *Science* **340**, 1317-1320.

Sarafian A. R., Nielsen S. G., Marschall H. R., McCubbin F. M. and Monteleone B. D. (2014) Early accretion of water in the inner solar system from a carbonaceous chondrite-like source. *Science* **346**, 623-626.

Sarafian A. R., Hauri E. H., McCubbin F. M., Lapen T. J., Berger E. L., Nielsen S. G., Marschall H. R., Gaetani G. A., Righter K. and Sarafian E. (2017a) Early accretion of

water and volatile elements to the inner Solar System: evidence from angrites. *Philos. T. Roy. Soc. A* **375**, 20160209.

Sarafian A. R., John T., Roszjar J. and Whitehouse M. J. (2017b) Chlorine and hydrogen degassing in Vesta's magma ocean. *Earth Planet. Sci. Lett.* **459**, 311-319.

Sarafian A. R., Nielsen S. G., Marschall H. R., Gaetani G. A., Hauri E. H., Righter K. and Sarafian E. (2017c) Angrite meteorites record the onset and flux of water to the inner solar system. *Geochim. Cosmochim. Acta* **212**, 156-166.

Scott E. R. D. and Krot A. N. (2014) 1.2 - Chondrites and their components. In *Treatise on Geochemistry 2nd ed*. (eds. H. D. Holland and K. K. Turekian) Elsevier, Oxford. pp 65-137.

Selverstone J. and Sharp Z. D. (2011) Chlorine isotope evidence for multicomponent mantle metasomatism in the Ivrea Zone. *Earth Planet. Sci. Lett.* **310**, 429-440.

Sharp Z. D., Barnes J. D., Brearley A. J., Chaussidon M., Fischer T. P. and Kamenetsky V. S. (2007) Chlorine isotope homogeneity of the mantle, crust and carbonaceous chondrites. Nature 446, 1062-1065.

Sharp Z. D., Barnes J. D., Fischer T. P. and Halick M. (2010a) An experimental determination of chlorine isotope fractionation in acid systems and applications to volcanic fumaroles. *Geochim. Cosmochim. Acta* **74**, 264-273.

Sharp Z. D., Shearer C. K., McKeegan K. D., Barnes J. D. and Wang Y. Q. (2010b) The chlorine isotope composition of the Moon and implications for an anhydrous mantle. *Science* **329**, 1050-1053.

Sharp Z. D., Mercer J. A., Jones R. H., Brearley A. J., Selverstone J., Bekker A. and Stachel T. (2013) The chlorine isotope composition of chondrites and Earth. *Geochim. Cosmochim. Acta* **107**, 189-204.

Sharp Z. D, Williams J. T., Shearer C. K., Agee C. and McKeegan K. D. (2016) The chlorine isotope composition of Martian meteorites 2. Implications for the early solar system and the formation of Mars. *Meteorit. Planet. Sci.* **51**, 2111-2126.

Shearer C. K., Burger P. V., Neal C. R., Sharp Z. D., Spivak-Birndorf L., Borg L., Fernandes V. A., Papike J. J., Karner J., Wadhwa M., Gaffney A., Shafer J., Geissman J., Atudorei N. V., Herd C., Weiss B. P., King P. L., Crowther S. A. and Gilmour J. D. (2010) Non-basaltic asteroidal magmatism during the earliest stages of solar system evolution: a view from Antarctic achondrites Graves Nunatak 06128 and 06129. *Geochim. Cosmochim. Acta* **74**, 1172-1199.

Shearer C. K., Burger P. V., Papike J. J., Sharp Z. D. and McKeegan K. D. (2011) Fluids on differentiated asteroids: evidence from phosphates in differentiated meteorites GRA 06128 and GRA 06129. *Meteorit. Planet. Sci*. **46**, 1345-1362.

Stephant A., Remusat L., Thomen A. and Robert F. (2014) Reduction of OH contamination in quantification of water contents using NanoSIMS imaging. *Chem. Geol*. **380**, 20-26.

Stephant A., Garvie L. A. J., Mane P., Hervig R. and Wadhwa M. (2018) Terrestrial exposure of a fresh Martian meteorite causes rapid changes in hydrogen isotopes and water concentrations. *Sci. Reports* **8**, 12385.

Tartèse R. and Anand M. (2013) Late delivery of chondritic hydrogen into the lunar mantle: Insights from mare basalts. *Earth Planet. Sci. Lett.* **361**, 480-486.

Tartèse R., Anand M., Barnes J. J., Starkey N. A., Franchi I. A. and Sano Y. (2013) The abundance, distribution, and isotopic composition of Hydrogen in the Moon as revealed by basaltic lunar samples: Implications for the volatile inventory of the Moon. *Geochim. Cosmochim. Acta* **122**, 58-74.

Tartèse R., Anand M., Joy K. H. and Franchi I. A. (2014a) H and Cl isotope systematics of apatite in brecciated lunar meteorites Northwest Africa 4472, Northwest Africa 773, Sayh al Uhaymir 169, and Kalahari 009. *Meteorit. Planet. Sci.* **49**, 2266-2289.

Tartèse R., Anand M., McCubbin F. M., Elardo S. M., Shearer C. K. and Franchi I. A. (2014b) Apatites in lunar KREEP basalts: The missing link to understanding the H isotope systematics of the Moon. *Geology* **42**, 363-366.

Treiman A. H., Boyce J. W., Gross J., Guan Y. and Eiler J. M. (2014) Phosphate-halogen metasomatism of lunar granulite 79215: impact-induced fractionation of volatiles and incompatible elements. *Am. Mineral.* **99**, 1860-1870.

Usui T., Alexander C. M. O.'D., Wang J., Simon J. I. and Jones J. H. (2012) Origin of water and mantle-crust interactions on Mars inferred from hydrogen isotopes and volatile element abundances of olivine-hosted melt inclusions of primitive shergottites. *Earth Planet. Sci. Lett.* **357-358**, 119-129.

Wadhwa M. (2008) Redox conditions on small bodies, the Moon and Mars. *Rev. Mineral. Geochem.* **68**, 493-510.

Wang K., Day J. M. D., Korotev R. L., Zeigler R. A. and Moynier F. (2014) Iron isotope fractionation during sulfide-rich felsic partial melting in early planetesimals. *Earth Planet. Sci. Lett.* **392**, 124-132.

Webster J. D., Goldoff B. A., Flesch R. N., Nadeau P. A. and Silbert Z. W. (2017) Hydroxyl, Cl, and F partitioning between high-silica rhyolitic melts-apatite-fluid(s) at 50–200 MPa and 700–1000 °C. *Am. Mineral.* **102**, 61-74.

Weiss B. P. and Elkins-Tanton L. T. (2013) Differentiated planetesimals and the parent bodies of chondrites. *Ann. Rev. Earth Planet. Sci.* **41**, 529-560.

Williams G. J. and Gold T. (1975) Regolith stirring and exposure: 3-dimensional study. *Lunar Sci. Conf. VI*. Lunar Planet. Inst., Houston. pp. 869-871.

Zhang Y. (2010) Diffusion in Minerals and Melts: Theoretical Background. *Rev. Mineral. Geochem.* **72**, 5-59.

Zhou Q. Z., Yin Q. Z., Young E. D., Li X. H., Wu F. Y., Li Q. L., Liu Y. and Tang G. Q. (2013) SIMS Pb-Pb and U-Pb age determination of eucrite zircons at < 5μm scale and the first 50Ma of the thermal history of Vesta. *Geochim. Cosmochim. Acta* **110**, 152-175.

Zhou Q. Z., Yin Q. Z., Shearer C. K., Li X. H., Li Q. L., Liu Y., Tang G. Q. and Li C. L. (2018) U-Pb and Pb-Pb apatite ages for Antarctic achondrite Graves Nunataks 06129. *Meteorit. Planet. Sci.* **53**, 448-466.

Zolotov M. Y. and Mironenko M. V. (2007) Hydrogen chloride as a source of acid fluids in parent bodies of chondrites. *Lunar Planet. Sci. XXXVIII*. Lunar Planet. Inst., Houston. #2340 (abstr.)

Figure captions

Figure 1: Back-scatter electron images (BSE) of the studied GRA 06128 section (A) and of selected areas with phosphate assemblages (B-D). Locations corresponding to the detailed BSE images are indicated by black rectangles in A. Apatite and merrillite H isotope analyses are numbered using orange and red fonts, respectively, and apatite Cl isotope analyses are numbered using a blue font. The pink rectangle in C shows location of NanoSIMS imaging. Analysis numbers refer to those given in Tables 1-2 (Ap1-Mer1 in B, Ap2-Mer2 in C, Ap3-Mer3 in D). Cl-Ap: chlorapatite; Cpx: clinopyroxene; Mer: merrillite; Ol: olivine; Opx: orthopyroxene; Pl: plagioclase.

Figure 2: Calibrations derived from apatite standard analysis for (A) Cl and (B) F abundance determination, and (C) average $\delta^{37}Cl_{SMOC}$ value obtained on Crystal Lode Pegmatite Mine apatite standard Ap005 (bulk $\delta^{37}Cl_{SMOC}$ = 0.2‰). All error bars represent 2σ standard deviations and uncertainties. Uncertainties associated with calibration lines represent 95% confidence intervals.

Figure 3: δD_{SMOW} values obtained on merrillite and apatite in GRA 06128 reported against their H_2O content.

Figure 4: NanoSIMS images and profiles of the $^{12}C/^{18}O$, $^{16}O^{1}H/^{18}O$, $^{28}Si/^{18}O$, $^{35}Cl/^{18}O$, and $^{40}Ca^{19}F/^{18}O$ measured ionic ratios at the transition between merrillite and apatite. Data have been smoothed in 9 pixels × 9 pixels (0.7 μm × 0.7 μm) squares for element ratios and in 25 pixels × 25 pixels (2 μm × 2 μm) squares for Cl isotope ratio. The scale bar in all images represents 4 μm. The white dashed line in the $^{40}Ca^{19}F/^{18}O$ image shows the location of the profile data (averaged over a width of 10 pixels).

Figure 5: $^{1}H/^{18}O$ and $^{2}H/^{1}H$ ratios measured in GRA 06128 phosphates reported against the measured $^{12}C/^{18}O$ ratios.

Figure 6: Cl isotope data obtained in GRA 06128/9 compared with a range of Solar System objects. Diamonds and circles indicate bulk and apatite Cl isotope compositions, respectively. Data are from Sharp et al., 2007, 2010a, 2010b, 2013, 2016; Barnes et al., 2009; John et al., 2010; Selverstone and Sharp, 2011; Shearer et al., 2011; Tartèse et al., 2014a; Boyce et al., 2015; Barnes et al., 2016; Bellucci et al., 2017; Sarafian et al., 2017b; Potts et al., 2018.

Figure 7: GRA 06128 phosphates δD_{SMOW} values reported against the inverse of their H_2O content. Modelling curves show the effect of (i) δD increase due to H loss as protons and deuterons from apatite, as modelled by Rayleigh distillation, and of (ii) adding 2-10 ppm H_2O characterised by δD values between 15000‰ and 4000‰, respectively, to phosphate initially containing 20-80 ppm H_2O during merrillite to apatite transformation.

Tables

Table 1: Water content and D/H ratios measured on phosphates in GRA 06128.

Analysis #	H_2O (ppm)	2σ (ppm)	D/H measured	*f* (%)[a]	D/H bckg corrected[b]	δD_{SMOW} (‰)	2σ (‰)
Apatite							
GRA06128_Ap1#1	23.6	0.6	4.49E-04	59	4.85E-04	1234	397
GRA06128_Ap1#3	31.0	0.8	5.06E-04	66	5.64E-04	1594	358
GRA06128_Ap1#4	19.0	0.5	5.02E-04	54	5.93E-04	1728	424
GRA06128_Ap1#5	27.5	0.7	3.16E-04	63	2.69E-04	239	441
GRA06128_Ap2#1	19.9	0.5	5.31E-04	55	6.41E-04	1949	397
GRA06128_Ap2#2	24.2	0.6	4.77E-04	60	5.31E-04	1445	393
GRA06128_Ap2#3	23.8	0.6	4.55E-04	60	4.95E-04	1277	393
GRA06128_Ap2#4	29.5	0.7	4.12E-04	65	4.21E-04	935	376
GRA06128_Ap3#1	51.5	1.3	3.32E-04	76	3.12E-04	435	368
GRA06128_Ap3#2	52.6	1.3	2.80E-04	76	2.44E-04	122	390
Merrillite							
GRA06128_Mer1#1	19.5	0.5	2.69E-04	55	1.63E-04	-249	496
GRA06128_Mer1#2	21.1	0.5	2.16E-04	57	7.72E-05	-645	531
GRA06128_Mer1#3	22.5	0.6	2.84E-04	58	2.03E-04	-64	462
GRA06128_Mer2#1	22.3	0.6	3.70E-04	58	3.52E-04	619	424
GRA06128_Mer2#3	29.0	0.7	2.23E-04	64	1.26E-04	-421	469
GRA06128_Mer3#1	50.1	1.2	2.64E-04	76	2.21E-04	17	397
GRA06128_Mer3#2	55.0	1.3	2.36E-04	77	1.31E-04	-395	419
GRA06128_Mer4#1	25.0	0.6	1.92E-04	61	1.32E-04	-394	487

[a]Proportion of H emitted from phosphates.
[b]Phosphate D/H ratio, corrected from background contribution of H (see text for details).

Table 2: F-Cl abundances and Cl isotope ratios measured in apatite in GRA 06128.

Analysis	F (wt.%)	2σ (wt.%)	Cl (wt.%)	2σ (wt.%)	$\delta^{37}Cl$ (‰)	2σ (‰)	OH[a] (apfu)	Cl (apfu)	F (apfu)	sum (apfu)
Ap1#1	0.62	0.04	5.63	0.26	3.0	2.4	0.01	0.83	0.17	0.99
Ap1#2	0.66	0.04	5.60	0.26	2.7	2.4	0.00	0.82	0.18	1.00
Ap1#3	0.69	0.04	5.65	0.26	3.0	2.4	0.00	0.83	0.19	1.02
Ap1#4	0.71	0.04	5.59	0.26	3.0	2.4	0.00	0.82	0.19	1.02
Ap1#5	0.72	0.05	5.59	0.26	2.8	2.4	0.00	0.82	0.20	1.02
Ap1#6	0.75	0.05	5.56	0.26	2.7	2.4	0.00	0.82	0.21	1.02
Ap1#7	0.82	0.05	5.43	0.25	3.1	2.4	0.00	0.80	0.22	1.02
Ap2#1	0.76	0.05	5.39	0.25	4.3	2.4	0.00	0.79	0.21	1.00
Ap2#2	0.70	0.04	5.58	0.26	3.5	2.4	0.00	0.82	0.19	1.01
Ap2#3	0.67	0.04	5.68	0.26	4.3	2.4	0.00	0.83	0.18	1.02
Average	0.71		5.57		3.2		0.00	0.82	0.19	1.01
±2SD	0.12		0.18		0.7		0.00	0.03	0.03	0.02

[a]OH component calculated by difference based on OH + Cl + F = 1 apfu.

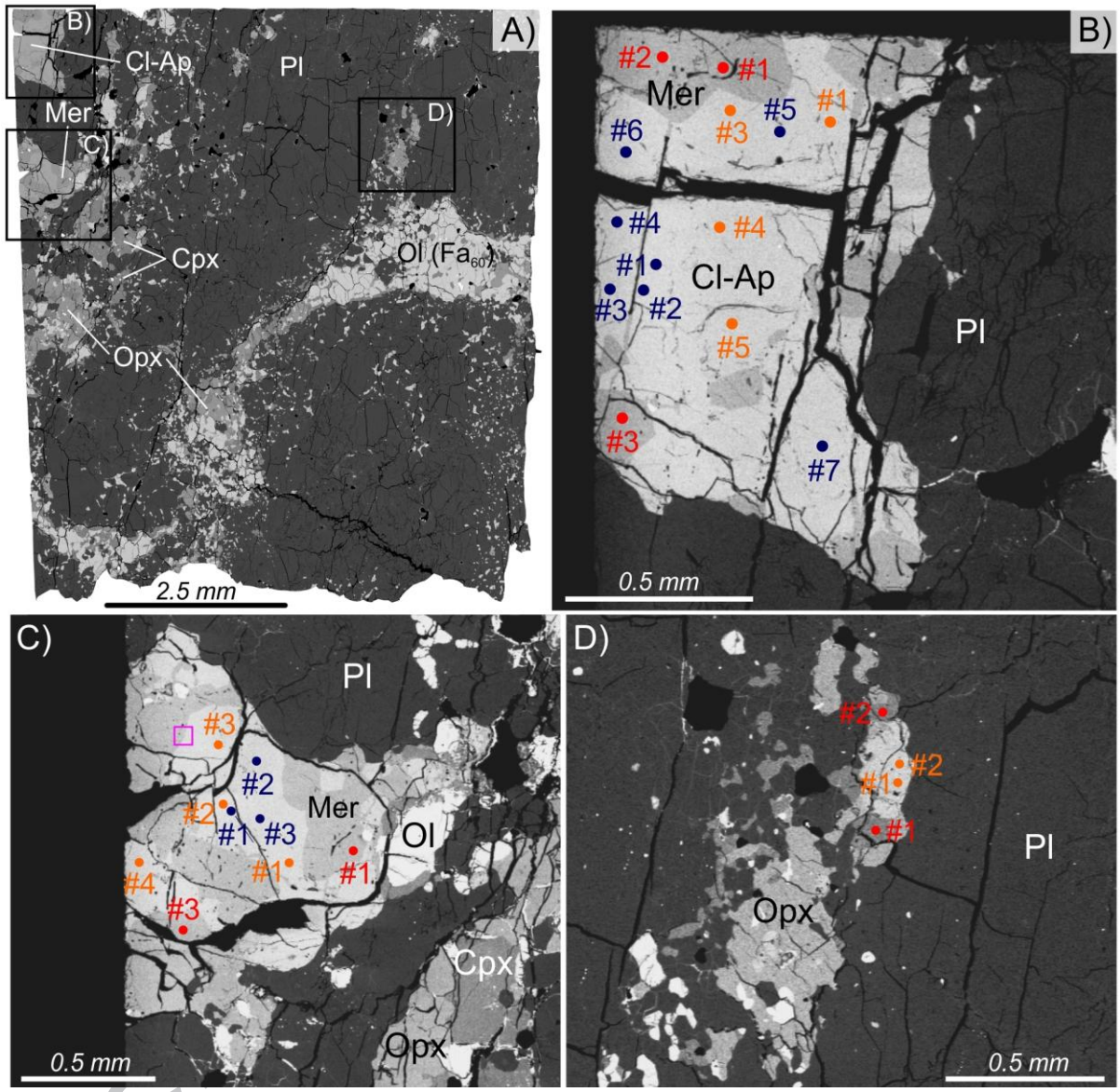
A)
B)
Cl-Ap
Pl
Mer
C)
D)
Cpx
Ol (Fa60)
Opx
2.5 mm
B)
#2
#1
Mer
#5
#1
#6
#3
#4
#4
#1
Cl-Ap
#3
#2
#5
Pl
#3
#7
0.5 mm
C)
Pl
#3
#2
#2
Mer
#1
#3
Ol
#4
#1
#1
#3
Cpx
Opx
0.5 mm
D)
#2
#2
#1
#1
Pl
Opx
0.5 mm